

Chapter 4

**Manipulating the ABCs of Self-Assembly via
Low- χ Block Polymer Design**

1. Chang, A. B.; Bates, C. M.; Lee, B.; Garland, C. M.; Jones, S. C.; Spencer, R. K.; Matsen, M. W.; Grubbs, R. H. Manipulating the ABCs of Self-Assembly via Low- χ Block Polymer Design. *Proc. Natl. Acad. Sci.* **2017**, *114*, 6462–6467.
2. Sunday, D. F.;* Chang, A. B.;* Liman, C. D.; Gann, E.; DeLongchamp, D. M.; Matsen, M. W.; Grubbs, R. H.; Soles, C. L. Evidence for Backbone Flexibility of Bottlebrush Block Copolymers Driven by Low- χ Assembly. **2018**. *submitted*. (*Corresponding authors.)

ABSTRACT

Molecular sequence and interactions dictate the mesoscale structure of all self-assembling soft materials. Block polymers harness this relationship to access a rich variety of nanostructured materials but typically require energetically unfavorable (high- χ) interactions between blocks. In this chapter, we demonstrate that the converse approach, encoding low- χ interactions in ABC bottlebrush triblock terpolymers ($\chi_{AC} \lesssim 0$), promotes organization into a unique mixed-domain lamellar morphology which we designate LAM_P. Transmission electron microscopy indicates that LAM_P exhibits ACBC domain connectivity, in contrast to conventional three-domain lamellae (LAM₃) with ABCB periods. Complementary small angle X-ray scattering experiments reveal an unusual trend: as the total polymer molecular weight increases, the domain spacing *decreases*. Self-consistent field theory reinforces these observations and predicts that LAM_P is thermodynamically stable below a critical χ_{AC} , above which LAM₃ emerges. Both experiments and theory expose close analogies to ABA' triblock copolymer phase behavior, collectively suggesting that low- χ interactions between chemically similar or distinct blocks intimately influence self-assembly. These conclusions provide new opportunities in block polymer design with potential consequences spanning all self-assembling soft materials.

Table of Contents

4-1	Introduction	92
4-2	Synthesis and Structure of Low- χ Block Polymers.....	93
4-3	Self-Consistent Field Theory	96
4-5	Decreasing Domain Spacing with Increasing Total Molecular Weight.....	99
4-6	Role of Low- χ Interactions	101
4-7	Molecular Asymmetry Effects.....	103
4-8	Screening Unfavorable Block-Block Interactions.....	105
4-9	Dispersity and Architecture	106
4-10	Evidence for Backbone Flexibility	107
4-11	Conclusions	117
4-12	References	117

4-1 Introduction

Block polymers are a diverse class of soft materials capable of self-assembling into complex periodic nanostructures. Synthetic command over composition, dispersity, sequence, and molecular architecture enables control over the mesoscopic order and macroscopic thermal, mechanical, rheological, and transport properties.¹⁻⁴ The phase behavior of “simple” linear AB diblock copolymers is universally parameterized by the segregation strength $\chi_{AB}N$ and relative volume fraction f , where χ_{AB} represents the effective Flory-Huggins binary interaction parameter and N is the total volume-averaged degree of polymerization. Mixing behavior, captured through the mean-field concept of χ_{AB} , is central to block polymer self-assembly: the competing demands of minimizing interfacial energy and maximizing configurational entropy only favor microphase separation when A-B interactions are repulsive ($\chi_{AB} > 0$).⁵⁻⁶ Extension to higher-order multiblock polymers introduces additional interaction parameters (χ_{ij}) that impact self-assembly and properties.⁷ For example, introducing a mutually incompatible C block ($\chi_{AC} > 0$, $\chi_{BC} > 0$) generates a host of new morphologies dictated by the chain connectivity (ABC, ACB, or BAC) and intrinsic χ_{ij} values.⁸⁻⁹ In this rich phase space, designing multiblock polymers with a combination of miscible and immiscible blocks can also access new structures and impart useful functions.¹⁰⁻¹¹ Perhaps the best known examples of such systems are linear ABA' triblock copolymers ($\chi_{AB} > 0$, $\chi_{AA'} \approx 0$): their high-value industrial applications as thermoplastic elastomers are entirely enabled by A/A' mixing and chain connectivity, which together create physically crosslinked materials with excellent processability and

mechanical properties.¹² The self-assembly of yet more complex systems, including ABA'C tetrablock polymers¹³⁻¹⁴ and $A_n(BA')_m$ heteroarm star polymers,¹⁵ is also crucially determined by A/A' miscibility. These examples illuminate interesting parallels and contrasts between block polymer phase behavior and protein self-assembly. Nature delivers exquisite control over protein folding by precisely tailoring amino acid sequences and intramolecular interactions that are often attractive (*e.g.*, hydrogen bonding), while block polymer design to date exploits simple molecular connectivity and primarily repulsive interactions ($\chi > 0$) to induce microphase separation.

Previous reports have investigated the role of negligible ($\chi \approx 0$) or attractive ($\chi < 0$) intermolecular interactions on the phase behavior of various homopolymer (AB/A')¹⁶⁻¹⁷ and block polymer (AB/A'C)¹⁸⁻¹⁹ blends. In contrast, studies in which the macromolecules themselves are intramolecularly encoded with miscible blocks are to the best of our knowledge limited to the aforementioned A/A' self-similar interactions. In this report, we study ABC bottlebrush triblock terpolymers with grafted poly(D,L-lactide), poly(styrene), and poly(ethylene oxide) side chains (LSO), featuring low- χ interactions ($\chi_{AC} \lesssim 0$) between distinct A and C end blocks. These materials generate a unique mixed morphology with atypical mesoscopic domain connectivity, which we denote LAMP. Additionally, under certain conditions of molecular asymmetry, another consequence of low- χ design manifests in decreasing domain spacing with increasing total molecular weight. Valuable insight into the molecular origins of this unusual behavior is achieved by comparison with analogous ABA' brush triblock copolymers – grafted poly(D,L-lactide)-*block*-poly(styrene)-*block*-poly(D,L-lactide) (LSL') – and self-consistent field theory (SCFT). The experimental and theoretical conclusions described herein regarding low- χ block polymers reveal unexpected breadth in self-assembly and should create new opportunities for molecular and materials design.

4-2 Synthesis and Structure of Low- χ Block Polymers

ABC and ABA' brush triblock polymers containing grafted poly(D,L-lactide) (PLA, A block), polystyrene (PS, B block), and poly(ethylene oxide) (PEO, C block) side chains were synthesized by ring-opening metathesis polymerization (ROMP).²⁰⁻²² The living

nature and synthetic utility of ROMP enable the formation of well-defined block polymers with precisely controlled molecular weight, narrow molecular weight dispersity, and diverse pendant functionalities. Figure 4.1 illustrates the molecular structure of the LSO and LSL' brush triblock polymers studied herein and highlights the relative interaction parameters dictated by block chemistry and sequence. Both LSO and LSL' feature low- χ interactions between the end blocks ($\chi_{AC}, \chi_{AA'} \lesssim 0$), which in particular distinguish LSO from typical frustrated ABC triblock polymers that include similar relative χ values but highly unfavorable A/C interactions ($\chi_{AC} \gg 0$).^{9,23} $N_A, N_B,$ and (N_C or $N_{A'}$) indicate the number-average degrees of polymerization through the polynorbornene backbone for blocks containing PLA, PS, and (PEO or PLA) grafts, respectively. Characterization data for all LSO and LSL' samples are provided in Tables 4.1 and 4.2, respectively. Synthetic details (Schemes C.1–C.2) and size-exclusion chromatograms (Figures C.1–C.3) for all samples are provided in Appendix C.

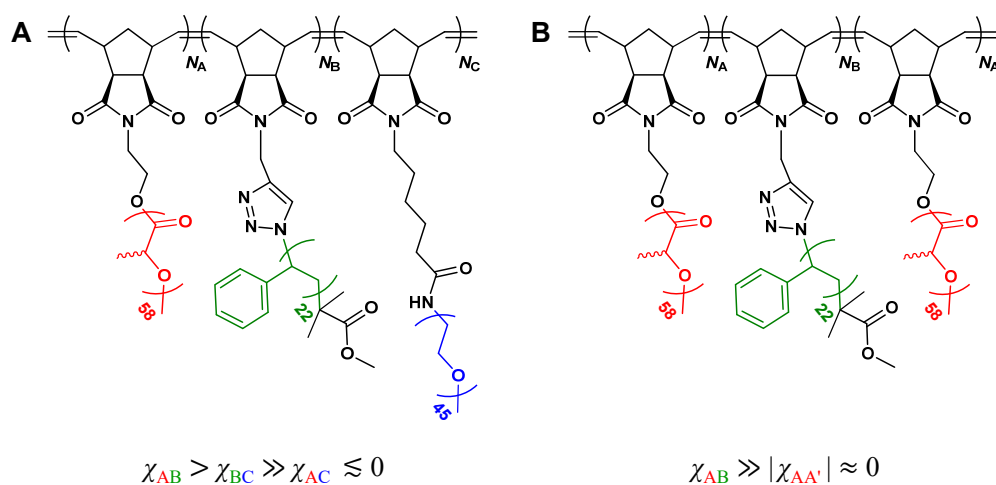


Figure 4.1: Molecular structures and relative interaction parameters for (A) LSO and (B) LSL' brush triblock polymers.

Table 4.1: Molecular composition and characterization data for all LSO samples. Samples are identified as LSO* or LSO- N_C (fixed N_A and N_B and variable N_C). For each block i , N_i indicates the number-average degrees of polymerization through the backbone and f_i indicates the volume fraction (estimated using values in Table C.1).

Sample ^a	N_A^b	N_B^b	N_C^b	f_A^c	f_B^d	f_C^e	M_n (kDa)	\bar{D} (M_w/M_n)
LSO*	28	27	5	0.57	0.37	0.06	203.2	1.02
LSO-0	26	24	0	0.61	0.39	0.00	178.4	1.00
LSO-2	26	24	2	0.60	0.38	0.02	182.9	1.01
LSO-4	26	24	4	0.58	0.37	0.05	187.5	1.01
LSO-6	26	24	6	0.57	0.36	0.07	192.0	1.00
LSO-8	26	24	8	0.56	0.35	0.09	196.6	1.00
LSO-10	26	24	10	0.54	0.35	0.11	201.1	1.00
LSO-12	26	24	12	0.53	0.34	0.13	205.7	1.01
LSO-14	26	24	14	0.52	0.33	0.15	210.2	1.01
LSO-16	26	24	16	0.51	0.32	0.17	214.8	1.07
LSO-20	26	24	20	0.49	0.31	0.20	223.9	1.00

Table 4.2: Molecular composition and characterization data for LSL'- N_A' series (fixed N_A and N_B and variable N_A'). For each block i , N_i indicates the number-average degrees of polymerization through the backbone and f_i indicates the volume fraction (estimated using values in Table C.1).

Sample ^a	N_A^b	N_B^b	$N_{A'}^b$	f_A^c	f_B^d	$f_{A'}^e$	M_n (kDa)	\bar{D} (M_w/M_n)
LSL'-0	30	28	0	0.61	0.39	0.00	206.6	1.01
LSL'-2	30	28	2	0.58	0.37	0.05	217.2	1.01
LSL'-5	30	28	5	0.56	0.35	0.09	227.8	1.05
LSL'-7	30	28	7	0.53	0.34	0.13	238.4	1.03
LSL'-10	30	28	10	0.51	0.33	0.16	248.9	1.02
LSL'-12	30	28	12	0.49	0.31	0.20	259.5	1.03
LSL'-14	30	28	14	0.47	0.30	0.23	270.1	1.02
LSL'-17	30	28	17	0.45	0.29	0.26	280.7	1.02
LSL'-19	30	28	19	0.44	0.28	0.28	291.3	1.03
LSL'-24	30	28	24	0.41	0.26	0.33	312.5	1.03

4-3 Self-Consistent Field Theory

Self-consistent field theory (SCFT), generally regarded as the state of the art for block polymer melts,²⁴ was used to model our polymers and provide insight into their self-assembly. The standard model for branched polymers was modified to account for the strong steric interactions that occur in bottlebrushes due to the high grafting density of the side chains, as was done previously for similar bottlebrush diblock copolymers.²⁵ Gaussian chains were used to represent the $N_b = N_A + N_B + N_C$ (LSO) or $N_b = N_A + N_B + N_{A'}$ (LSL') side chains, and the volumes and unperturbed end-to-end lengths of the side chains were set to known literature values.²⁶⁻²⁷ For the backbone, a worm-like chain of fixed persistence length was employed to handle the strong lateral tension that occurs due to side chain crowding. The interactions between the three side chain species (PLA, PS, and PEO) were represented in the Hamiltonian by standard Flory-Huggins terms controlled by χ_{LS} , χ_{SO} , and χ_{LO} . The equilibrium lamellar period (d^*) was obtained by minimizing the free energy (F). Figure 4.2 provides a schematic of chain dimensions. Additional SCFT details, including values for input parameters (Table C.1), are provided in Appendix C-3.

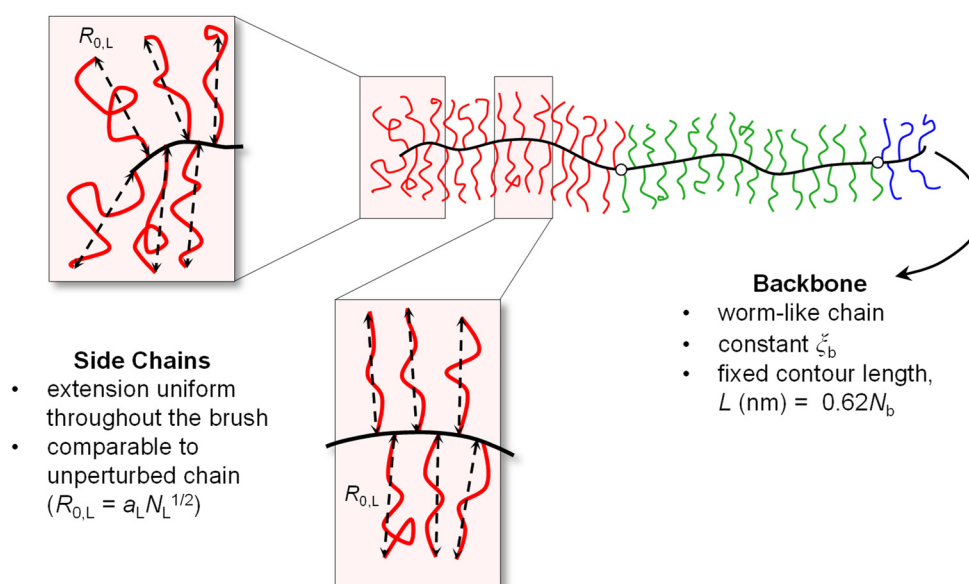


Figure 4.2: Schematic of realistic LSO* chain dimensions used in SCFT calculations. The side chains are not expected to extend significantly more than their unperturbed end-to-end distance $R_{0,\gamma} = a_\gamma N_\gamma^{1/2}$ (where a_γ is the statistical segment length and N_γ is the degree of polymerization of $\gamma = L, S, \text{ or } O$). The backbone is treated as a worm-like chain of constant persistence length ξ_b and fixed contour length L .

4-4 Unique Domain Connectivity: LAM_P

We begin by presenting data and calculations corresponding to LSO brush triblock terpolymers (Figure 4.1A), then draw close analogies to LSL' (Figure 4.1B) phase behavior. All materials self-assemble into well-ordered lamellar morphologies. Transmission electron micrographs of thin sections of LSO* ($N_A = 28$, $N_B = 27$, $N_C = 5$) stained over ruthenium tetroxide (RuO_4) vapor reveal a three-color, four-layer lamellar morphology (Figure 4.3A). (Additional images are provided in Appendix C, Figure C.4)

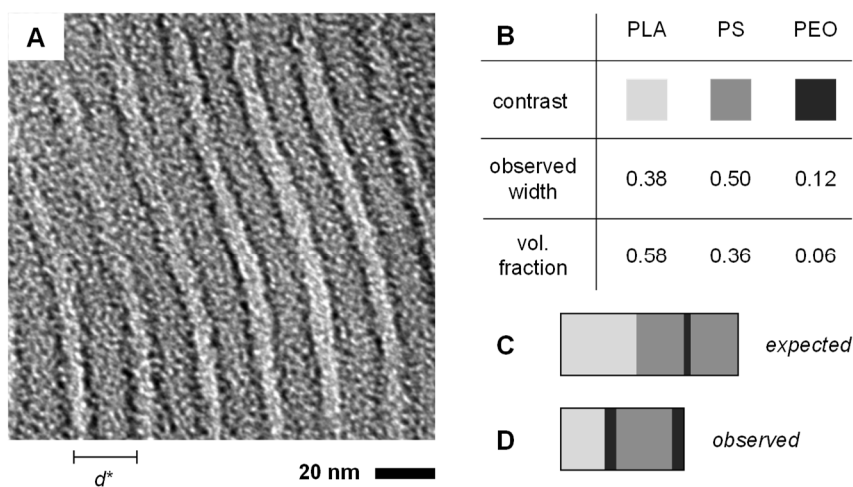


Figure 4.3: (A) TEM of LSO* stained with RuO_4 . (B) Relative contrast from the stain, relative widths of corresponding layers observed by TEM, and side chain volume fractions measured by ^1H NMR. (C) One LAM_3 period with the expected ABCB domain connectivity and layer widths based on data in (B). (D) One LAM_P period observed in (A), exhibiting mesoscopic ACBC domain connectivity.

Exposing L, S, and O to RuO_4 vapor results in unstained, slightly stained, and strongly stained domains respectively, as deduced from literature results: PS is selectively stained in PLA/PS mixtures,²⁸⁻²⁹ and PEO is stained to a greater extent than PS.³⁰⁻³¹ Surprisingly, the extent of staining and layer widths observed by TEM are completely inconsistent with both the side chain volume fractions measured by ^1H NMR ($f_L = 0.57$, $f_S = 0.37$, $f_O = 0.06$) (Figure 4.3B) and the ABCB connectivity required by the expected three-domain microstructure, LAM_3 (Figure 4.3C).⁸⁻⁹ The conflict between LAM_3 and the pattern observed by TEM can only be resolved by invoking partial mixing between the A and C end blocks, apparently driven by low- χ interactions ($\chi_{AC} \lesssim 0$). The resulting morphology exhibits mesoscopic ACBC connectivity (Figure 4.3D), consistent with the observed

staining pattern. Since the three blocks are not well-segregated, the side chain volume fractions are not required to equal the relative domain widths. Reflecting the crucial role of partial mixing, this new morphology is herein designated LAMP.

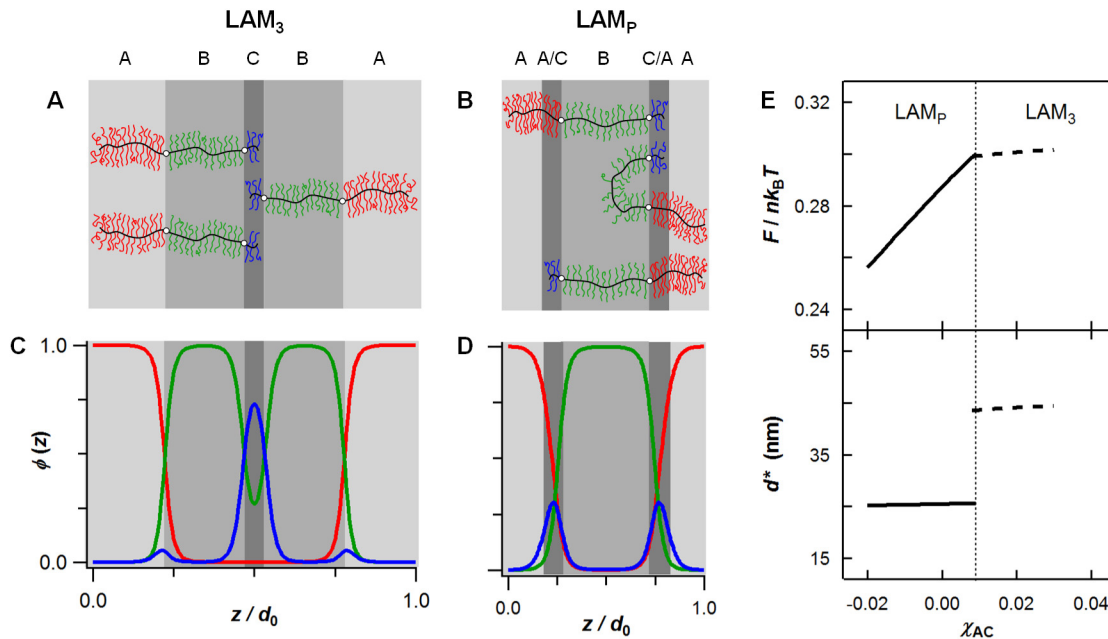


Figure 4.4: Illustrations and SCFT data distinguishing LAM₃ and LAMP morphologies. In *A–D*, the light, medium, and dark gray layers represent PLA, PS, and PEO (or mixed PLA/PEO) domains, respectively. (*A*, *B*) LSO chain packing in (*A*) LAM₃ and (*B*) LAMP. (*C*, *D*) SCFT composition profiles for LSO* within one normalized lamellar period (z/d_0), where $\phi(z)$ is the relative segment concentration of each component. (*C*) $\chi_{AC} > \chi^C$: LAM₃ with $d^* = 43.5$ nm. (*D*) $\chi_{AC} < \chi^C$: LAMP with $d^* = 25.6$ nm. (*E*) SCFT calculations of the normalized free energy (*top*) and domain spacing (*bottom*) versus $\chi_{AC} \equiv \chi_{LO}$ for LSO*. The transition from mixed (LAMP) to unmixed (LAM₃) morphologies is first-order, occurring at a critical value χ^C (dotted line); for $\chi_{AB} = 0.080$ and $\chi_{BC} = 0.049$, $\chi^C = 0.009$.

SCFT fully supports the distinction between LAM₃ (Figure 4.4A) and LAMP (Figure 4.4B), controlled primarily by the relative and absolute interaction parameters. Composition profiles for LSO* were calculated over one lamellar period using realistic PLA-PS ($\chi_{AB} \equiv \chi_{LS}$) and PS-PEO ($\chi_{BC} \equiv \chi_{SO}$) values estimated in the literature: $\chi_{LS} = 0.080$ ³² and $\chi_{SO} = 0.049$ ³³ at 140 °C, renormalized to a common monomer reference volume (118 Å³). (We note that literature χ values obtained by fitting experimental data to mean-field approximations are often inaccurate, potentially affecting the agreement between experiment and theory.³⁴) PLA-PEO interactions ($\chi_{AC} \equiv \chi_{LO}$) were arbitrarily varied in the

simulations, and LAM₃ is correctly predicted to occur at moderate to large χ_{AC} (Figure 4.4C), in broad agreement with previous experimental and theoretical studies of frustrated ABC triblock terpolymers.³⁵⁻³⁷ In contrast, LAM_P exclusively emerges when χ_{AC} is sufficiently small to favor partial A/C block-block mixing (Figure 4.4D). Using this collection of physical parameters, a first-order phase transition between LAM₃ and LAM_P was predicted to occur at a critical value $\chi^C = 0.009$ (Figure 4.4E). The mesoscopic ACBC domain connectivity and relative domain widths predicted for LAM_P perfectly match the pattern observed in Figure 4.3A and reinforce the microscopic origins of mixing deduced from TEM.

4-5 Decreasing Domain Spacing with Increasing Total Molecular Weight

A series of LSO brush triblock terpolymers with fixed $N_A = 26$ and $N_B = 24$ (guaranteed by a common parent diblock) and variable N_C (Scheme C.2) highlights additional consequences of block-block mixing. N_C was varied in increments of two or four backbone repeat units, from $N_C = 0$ (LSO-0) to $N_C = 20$ (LSO-20) (Table 4.1). (Note that, due to the high molecular weight of each PEO macromonomer, the total molecular weight varies by >45,000 g/mol across this series.)

All samples were annealed at 140 °C under modest applied pressure, and the ordered structures that developed were identified by synchrotron small-angle X-ray scattering (SAXS). (See Appendix C-5 for further information.) SAXS measurements reveal an unusual trend: as the total molecular weight (M) increases over the range of compositions where LAM_P forms ($0 < f_O \leq 0.20$), the lamellar period (d^*) strongly *decreases*: $d^* \sim M^{-0.87}$ (Figure 4.5). For comparison, Figure 4.5 also includes literature data for linear poly(isoprene-*b*-styrene-*b*-ethylene oxide) (ISO) and poly(styrene-*b*-isoprene-*b*-ethylene oxide) (SIO) triblock terpolymers similarly synthesized by varying the O block length from a common parent diblock. The domain spacing trends observed for both ISO and SIO series typify the expected increase in lamellar period with increasing M : $\alpha_{ISO} \approx 0.90$ ³⁸⁻³⁹ and $\alpha_{SIO} \approx 0.56$.⁴⁰ Clearly, α_{LSO} is strikingly different. Additional data illustrating the unusual negative trend for LSO are summarized in Appendix C-6, Table C.2. Schematic illustrations of assigned structures (Figure C.5), indexed 2D SAXS data

(Figure C.6), 1D azimuthally averaged intensity reductions (Figure C.7), and TEM images (Figure C.8) are also provided.

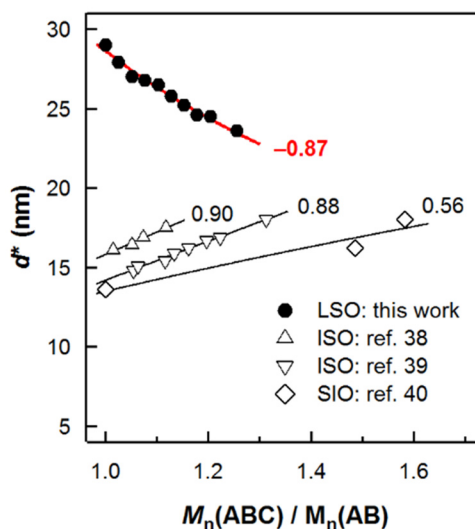


Figure 4.5: Lamellar periods (d^*) versus normalized molecular weight for brush LSO (this work) and linear ISO and SIO triblock terpolymers (literature data). Calculated exponents (best fit) to the power law $d^* \sim M^\alpha$ are included for comparison.

A series of LSL' brush triblock copolymers was similarly synthesized from identical macromonomers, generating an analogous series with variable end block length from a parent LS diblock ($N_A = 30$, $N_B = 28$). Like LSO, this LSL' series exhibits decreasing lamellar periods with increasing end block length (*i.e.*, increasing total molecular weight) (Figure 4.6A). Additional morphological data for LSL' are provided in Appendix C-7 (Table C.3 and Figures C.9–C.10). Differential scanning calorimetry (DSC) data for LSL' and LSO are compared in Figure 4.6B and provide quantitative evidence of block-block mixing in LSO. For all LSO samples, a single glass transition temperature (T_g) was observed between $T_{g,PLA}$ (55 °C) and $T_{g,PEO}$ (−70 °C) (Appendix C-8, Figure C.11). As N_C (and therefore the weight fraction of PEO) increases, T_g decreases, consistent with continued dilution of mixed A/C domains by the low- T_g component. The presence of only one T_g in polymer blends is generally regarded as evidence for miscibility⁴¹⁻⁴² and is consistent with the behavior of PLA and PEO homopolymers, which mix over wide ranges of molecular weights and blend compositions.⁴³⁻⁴⁴ In the analogous LSL' series, a single T_g

corresponding to the PLA block is observed that does not change as N_A increases, since mixed domains inherently remain pure PLA (Figure C.12).

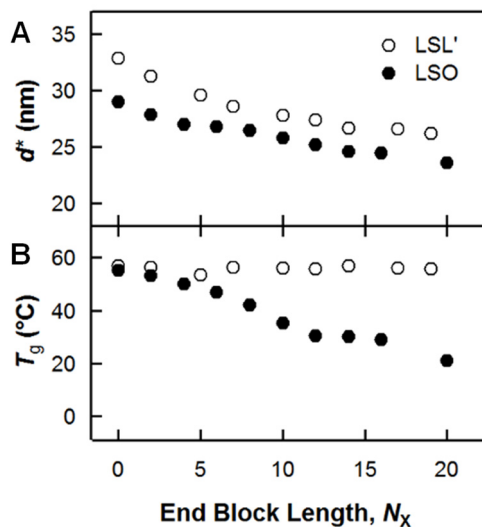


Figure 4.6: Consequences of varying end block length N_X in LSL' and LSO. (A) Domain spacing d^* . (B) Apparent PLA glass transition temperatures (T_g); for all samples, a single T_g ($T_{g,PEO} < T_g \leq T_{g,PLA}$) was observed.

4-6 Role of Low- χ Interactions

We have investigated herein the impact of low- χ block-block interactions on structure and physical properties by studying densely grafted ABC and ABA' brush triblock polymers. The LSO polymers described above self-assemble into lamellae with unique domain connectivity (ACBC), which we denote LAM_P. In contrast, linear ABC triblock terpolymers (*e.g.*, ISO and SIO) have been extensively studied and typically form two- or three-domain lamellar morphologies (LAM₂ or LAM₃) depending on block lengths and relative interaction parameters. In the conventional LAM₃ morphology generated by both ISO and SIO, the mesoscopic domain connectivity (ABCB) necessarily reflects the underlying molecular sequence. In other words, the self-assembly of ABC... multiblock polymers into lamellae (*i.e.*, structures periodic in one dimension) typically requires A, B, C, ... domains to be connected in that order due to the covalent linkages between blocks. The crucial differences distinguishing LSO and ostensibly similar ISO/SIO triblocks could potentially be attributed to either the polymer architecture (brush vs. linear) or block-block

interactions. We note that architecture-induced segmental mixing has been demonstrated in ABC heteroarm star terpolymers, wherein forming low-energy morphologies may force one arm to transit across an incompatible domain ($\chi > 0$).⁴⁵⁻⁴⁶ However, these architecture effects do not pertain to brush LSO since the blocks are connected end-to-end in the same way as linear ABC triblock terpolymers. The data presented in Figures 4.3–4.6 instead indicate that block-block interactions, captured through the mean-field concept of Flory-Huggins binary interaction parameters (χ_{ij}), are the dominant factors governing the unique behavior of LSO.

Both the relative *and* absolute magnitudes of each χ_{ij} , convolved with the molecular sequence, underpin the self-assembly of multiblock polymers. For example, given I, S, and O blocks with $\chi_{IO} > \chi_{IS} \approx \chi_{SO}$,⁴⁷⁻⁴⁸ SIO connectivity imposes costly high- χ interactions between adjacent blocks ($\chi_{BC} > \chi_{AB} \approx \chi_{AC}$), while ISO connectivity alleviates this penalty by not inherently requiring I/O (A/C) interfaces. ISO and SIO phase diagrams are consequently distinct due to so-called frustration. The influence of each χ_{ij} is less understood. In contrast to (SI/IS)O materials where every $\chi_{ij} \gg 0$, the LSO polymers studied herein feature low χ_{AC} between the end blocks ($\chi_{LO} \lesssim 0$). Actual literature estimates for χ_{LO} range from 0.0038 to -0.161 depending on end groups and measurement techniques.⁴⁹⁻⁵⁰ Combining any $-0.161 < \chi_{LO} < 0.0038$ with the aforementioned literature values $\chi_{LS} = 0.080$ and $\chi_{SO} = 0.049$ yields a frustrated system. SCFT simulations (Figure 4.4) suggest that the magnitude of χ_{LO} , beyond simple frustration effects, dictates the unique LAM_P self-assembly observed in Figure 4.3. Calculations for LSO indicate that LAM_P is stable when $\chi_{LO} < \chi^C$, which marks a first-order phase transition between LAM_P and LAM₃ (Figure 4.4E). The predicted value of χ^C is sensitive to physical parameters including the statistical segment lengths and χ_{ij} and is consequently difficult to quantitatively associate with experiments. Using the aforementioned literature values corresponding to L, S, and O pairwise interactions, we estimate $\chi^C \approx 0.009$, which sets an approximate upper bound on the value of χ_{LO} since no evidence of LAM₃ is experimentally observed. Experiment and theory collectively suggest that low- χ interactions ($\chi_{AC} \lesssim 0$) underpin the self-assembly of LSO to LAM_P.

4-7 Molecular Asymmetry Effects

The pronounced decrease in domain spacing observed for LSO and LSL' upon increasing N_C or $N_{A'}$ (at constant N_A, N_B) also emerge as consequences of the low- χ design, involving molecular asymmetry, block-block mixing, and screening effects. SCFT simulations of linear ABA' triblock copolymers have previously revealed that asymmetry in A/A' block lengths can induce a decrease in domain spacing.⁵¹ The explanation is twofold. First, A/A' asymmetry lowers the stretching energy in A domains,⁵² which can be understood by imagining equivalent A block lengths and then transferring material from one end to the other; as asymmetry increases, the overall A segment distribution shifts away from the interface, increasing d^* . Second, when the end blocks are sufficiently asymmetric, a significant proportion of the shorter A blocks can pull out into B domains (Figure 4.7A). Although chain pullout incurs an enthalpic penalty ($\chi_{AB} > 0$), this effect is more than compensated by relaxation of the B block, which is entropically favored and further increases d^* . The synthesis of ABA' triblocks from a common diblock precursor exhibits the same trend: growing longer A' blocks decreases molecular asymmetry and correspondingly lowers d^* . Experimental studies of linear ABA' triblock copolymers have corroborated this theory of end block asymmetry,⁵³⁻⁵⁴ and the LSL' and LSO brush triblock polymers studied herein exhibit strikingly similar behavior. We conclude that architecture is not a critical molecular design parameter dictating the trends in d^* (Figures 4.5–4.6); instead, the close parallels between the self-assembly of ABA' triblock copolymers and appropriately designed ABC triblock terpolymers implicate block-block mixing. ABA' samples (linear or brush) clearly have mixed A/A' domains before chain pullout, and a negligible χ_{LO} in LSO should also promote end block mixing. Application of the stretching energy and chain pullout concepts developed to rationalize ABA' self-assembly therefore also captures the essence of ABC systems (Figure 4.7B). Molecular weight dispersity additionally favors pullout of shorter end blocks (A' or C), while longer ones remain anchored in mixed domains.

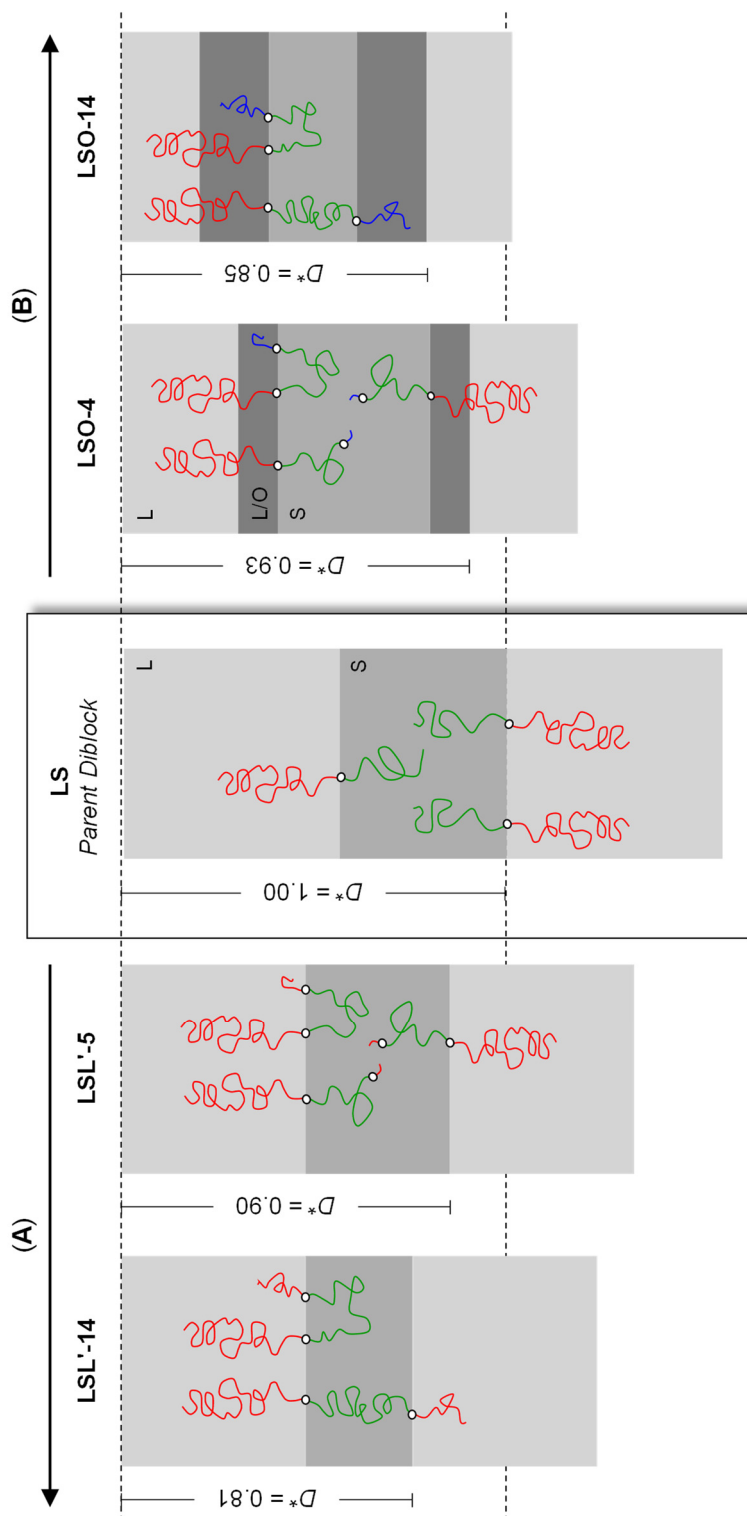


Figure 4.7: Illustration of chain pullout to explain the trends in d^* for LSL' and LSO brush triblock polymers with varying end block length (equivalently, varying molecular asymmetry). Linear chains are depicted to aid visualization. As the end block length N_x increases from a fixed parent LS diblock, d^* decreases (here, $D^* \equiv d^*/d_{LS}^*$ where d_{LS}^* is the period of the parent LS diblock). (A) X = A' (LSL'): short PLA end blocks pull out of PLA domains into PS domains. (B) X = C (LSO): short PEO end blocks pull out of mixed PLA/PEO domains into PS domains.

Informed SCFT simulations of LSO indicate the stability of LAM_P over a wide range of N_C (Appendix C-9, Figure C.13). In addition, simulations incorporating an exponential distribution of end block dispersity for both LSO and LSL' (Tables C.4–C.5) show good agreement between the predicted and measured magnitudes of d^* . The simulations capture a sharp initial decrease in d^* when the backbone lengths of the third block are short ($N_C, N_{A'} \leq 7$), reinforcing the significance of molecular asymmetry and chain pullout. As the end block lengths continue to increase however, the predicted values of d^* monotonically increase, in contrast to the experimental trends. These disparities may reflect (1) inaccuracies in the χ_{ij} values employed,³⁴ (2) larger dispersities in N_C and $N_{A'}$ than anticipated by theory, or (3) potential non-equilibrium effects (Chapter 5-2).

4-8 Screening Unfavorable Block-Block Interactions

In LSO, the effects of molecular asymmetry and chain pullout are amplified by the screening of high- χ block-block interactions. The most unfavorable contacts in LSO (L/S) can be partially mitigated by inserting PEO between PLA and PS domains near the interface, since $\chi_{LS} > \chi_{SO}$ and $\chi_{LO} \lesssim 0$. This possibility is naturally permitted in the disordered state, but upon self-assembly to the conventional LAM₃ morphology, chain connectivity necessarily creates energetically costly PLA/PS interfaces. Screening L/S contacts in LAM₃ would typically require altering the block sequence to LOS, an impossible task post-synthesis, but LAM_P restores this opportunity by incorporating partial mixing between the end blocks. This phenomenon decouples the molecular block sequence from the self-assembled domain pattern. Screening unfavorable block-block interactions in LSO likely also contributes to the molecular origins of the domain spacing trend. As PEO inserts between PLA and PS blocks at the interface, it should expand the intermolecular distance in the plane of the lamellae and therefore contract the lamellar period (i.e., d^*). Similar mixing consequences have been observed in block polymer/homopolymer blends in which the homopolymer localizes at the block-block interfaces.⁵⁵⁻⁵⁷ Chapter 5 will discuss the phase behavior of blends of LS brush diblock copolymers with linear O homopolymers. Consequences of low- χ interactions manifest in blends as well as in LSO brush triblock terpolymers.

4-9 Dispersity and Architecture

Comparing LSO, LSL', and linear (IS/SI)O reinforces the importance of low- χ interactions and rejects other potential explanations for the unique mesoscopic ACBC domain connectivity and domain spacing trend. Dispersity differences among the blocks can be discounted since all samples across the LSO, LSL', ISO, and SIO series depicted in Figures 4.5–4.6 were synthesized by living polymerizations (either ROMP or anionic polymerization) from parent diblock precursors. Since O comprises the C block in each ABC series, PEO clearly does not inherently cause domain contraction with increasing O block lengths or weight fractions. Chapter 5 of this thesis will discuss crystallization and other potential effects associated with increasing PEO content

We expect that the phenomena described above, illustrating the physical consequences of designing polymers with certain miscible blocks, are general to the class of soft materials with $\chi_{AB}, \chi_{BC} \gg |\chi_{AC}| \approx 0$. Although bottlebrush polymers were employed in the present study, SCFT calculations predict identical behavior for analogous linear triblock terpolymers with the same absolute and relative χ parameters (Appendix C, Figure C.14). While bottlebrush polymers experience some steric-induced stiffening compared to linear polymers,⁵⁸⁻⁵⁹ our results suggest that brush LSO and LSL' are actually relatively flexible. The backbone flexibility should enable brush LS(O/L') to adopt looping midblock configurations (Figures 4.4 and 4.7), just like linear AB(C/A') triblocks with compatible end blocks.⁶⁰⁻⁶¹ Informed SCFT calculations indicate that the effective backbone persistence length of brush LSO and LSL' corresponds to approximately 5 norbornene repeat units.²⁵ Since the B midblocks of LSO and LSL' are much longer than 5 units ($N_B \geq 24$), they should readily form loops, although undoubtedly less than the 60% predicted for flexible (linear) triblocks.⁶² Our results, placed in the context of recent work on bottlebrush block polymer self-assembly, suggest that polymer architecture is not a major factor controlling the formation of partially mixed morphologies. Instead, the primary driving force appears to be the magnitude of χ_{AC} . Designed low- χ interactions emerge as tools to manipulate block polymer self-assembly.

4-10 Evidence for Backbone Flexibility

In the preceding sections, we proposed that the bottlebrush architecture should readily permit the formation of looping midblocks in brush LSO triblock terpolymers. However, loops demand significant curvature of the backbones, opposing the highly extended nature of bottlebrush polymers. Certain physical consequences of the relative stiffness of bottlebrush block polymers compared to linear analogues have been discussed in Chapter 3 of this thesis. For example, the scaling of the lamellar period with the total backbone degree of polymerization depends on the grafting density z , such that $d^* \sim N_{\text{bb}}^{\alpha(z)}$ and $\alpha \sim z$ (Chapter 3-3).⁶³ The apparent stiffness of bottlebrush polymers in these contexts raises interesting questions about the limits of backbone flexibility and the corresponding implications for physical properties. In order to address these questions, we further studied the unusual phase behavior of LSO brush triblock terpolymers using resonant soft X-ray reflectivity (RSoXR) and near edge X-ray fine structure absorption spectroscopy (NEXAFS). Insight from these measurements supports the assignment of a new partially mixed morphology (LAM_P) and provides unambiguous evidence for the backbone flexibility of bottlebrush polymers in both thin films and the melt.

Both RSoXR⁶⁴⁻⁶⁵ and NEXAFS⁶⁶⁻⁶⁷ take advantage of the sensitivity of soft X-rays to variations in chemical composition in order to evaluate the concentration — and in some cases, the orientation — of molecular bonds in a material. Near an atomic absorption edge, the complex index of refraction, $n(E) = 1 - \delta(E) + i\beta(E)$, varies significantly as a function of energy and molecular composition due to electronic transitions between occupied and unoccupied orbitals. This sensitivity to chemical structure can be used to tune the contrast between different components in soft materials, enabling the direct study of composition distributions in all-organic thin films.⁶⁸⁻⁷⁰ Whereas NEXAFS is primarily surface-sensitive, RSoXR can depth-profile the molecular composition of films up to several hundred nanometers thick depending on the X-ray energy. This exquisite chemical sensitivity over multiple length scales enable NEXAFS and RSoXR measurements of brush LSO thin films to probe the composition profile and brush backbone conformations.

Brush LSO samples were prepared by spin-coating thin films from propylene glycol methyl ether acetate (PGMEA) onto silicon wafers. Among the selected brush LSO triblock terpolymers, the backbone degrees of polymerization for the PLA and PS blocks were fixed

($N_A = 26$, $N_B = 24$) while the backbone degree of polymerization for the PEO block was varied ($N_C = 8, 12, 16, 20$) (Figure 4.8A). These samples correspond to LSO-8, LSO-12, LSO-16, and LSO-20 in Table 4.1. Reference samples corresponding to the constituent brush diblock polymers (SO and LS, Figure 4.8B) and homopolymers (L, S, O, and polynorbornene, Figure 4.8C) were also prepared. Transmission absorption measurements of these reference samples were used to evaluate the optical constants of each component toward correlating the measured scattering length density (SLD) with the chemical composition.

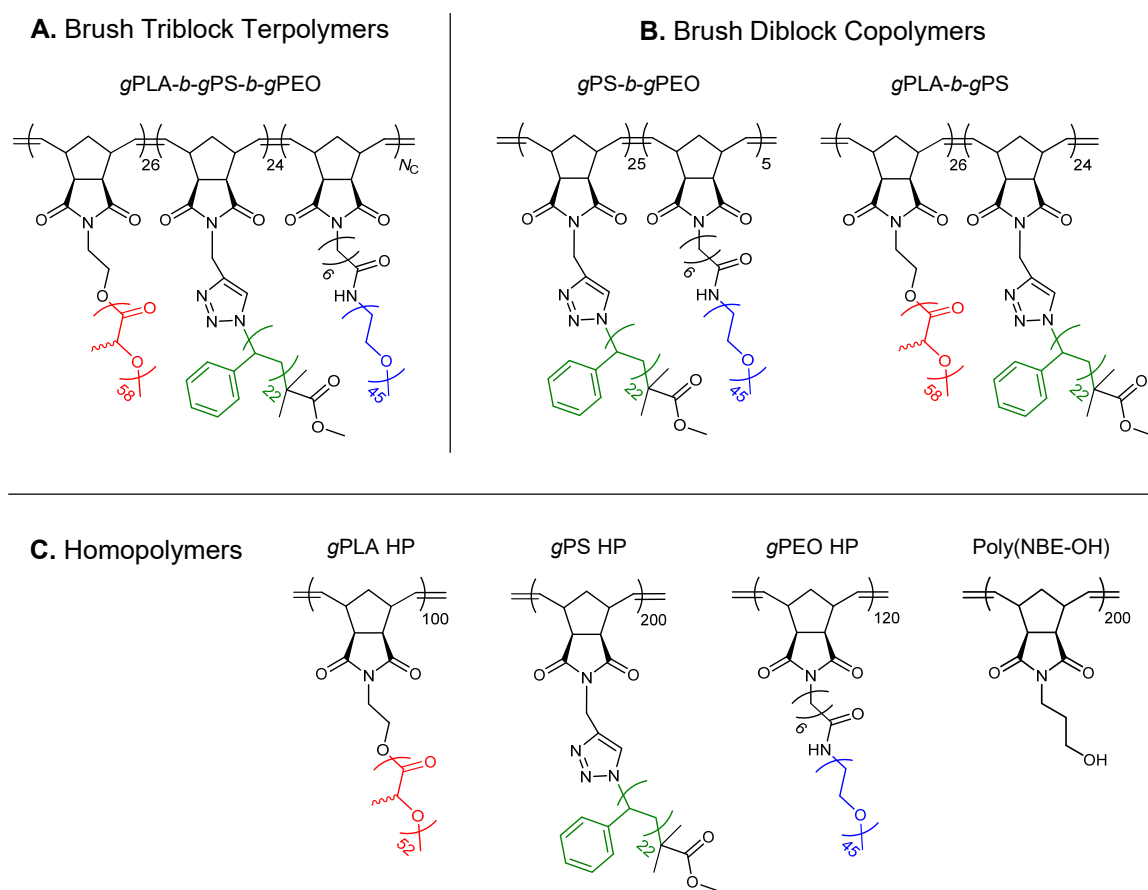


Figure 4.8: (A) Brush LSO triblock terpolymers samples prepared for reflectivity measurements: $N_C = 8, 12, 16, 20$ (Table 4.1). (B, C) Reference samples, including (B) brush diblock copolymers (SO and LS) and (C) homopolymers of each component (*i.e.*, brush PLA, brush PS, brush PEO, and the polynorbornene backbone).

Atomic force microscopy (AFM) confirms that all films are uniform and under 100 nanometers thick. Representative micrographs are shown in Figure 4.9. Under most conditions, the films dewetted, forming islands and holes that rendered the samples ill-suited for reflectivity measurements. Optimization of the annealing process achieved uniform thin films. Surprisingly, the commensurability conditions for the brush block polymers differed from the well-established conditions for linear analogues. For typical *linear* block polymers, lamellae form parallel to the substrate when the total film thickness is either a half-integer multiple of d^* (asymmetric wetting) or a full-integer multiple of d^* (symmetric wetting). In contrast, the LS and LSO block polymers assembled at $3.25d^*$. Further studies are underway in order to explore the impact of molecular architecture on the commensurability conditions.

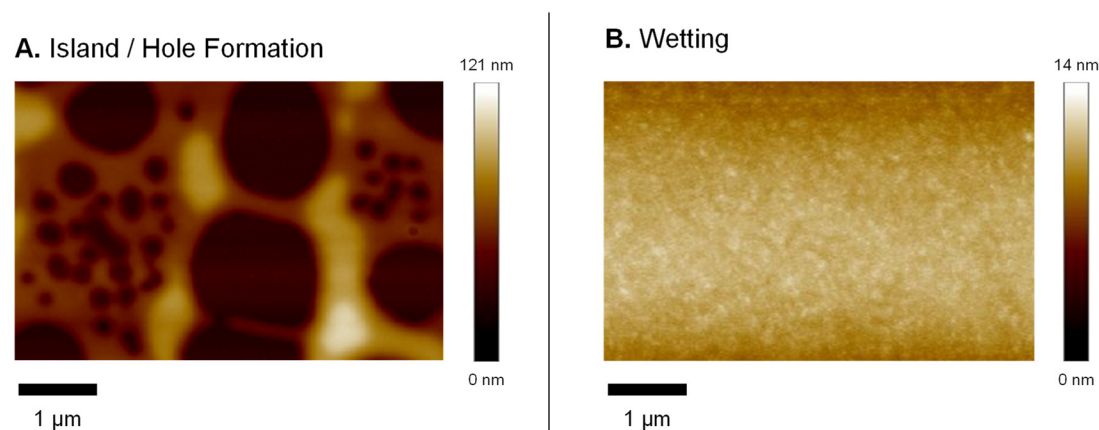


Figure 4.9: Representative atomic force micrographs (AFM) corresponding to spin-coated films of LSO-0 on silicon. (A) Under many conditions, the films dewetted, forming islands and holes. The commensurability conditions differ for brush and linear block polymers. (B) Under optimized conditions, the films wet the substrate.

Reflectivity measurements of the brush LSO films were conducted near the carbon edge in order to tune the contrast among the three components (L, S, and O). The experimental and simulated reflectivity data for LSO-12 ($N_C = 12$) are shown in Figure 4.10A. Measurements were performed at (1) 270 eV, which is effectively non-resonant and primarily sensitive to the electron density; (2) 284 eV, near the characteristic absorption peak for aromatic carbon-carbon bonds (≈ 285 eV) and therefore highly sensitive to PS blocks; and (3) 286 eV, near the characteristic absorption peak for carbonyl bonds (≈ 288 eV) and therefore highly sensitive to PLA blocks. Measurements at these three energies enable determination of the component distributions throughout the film.

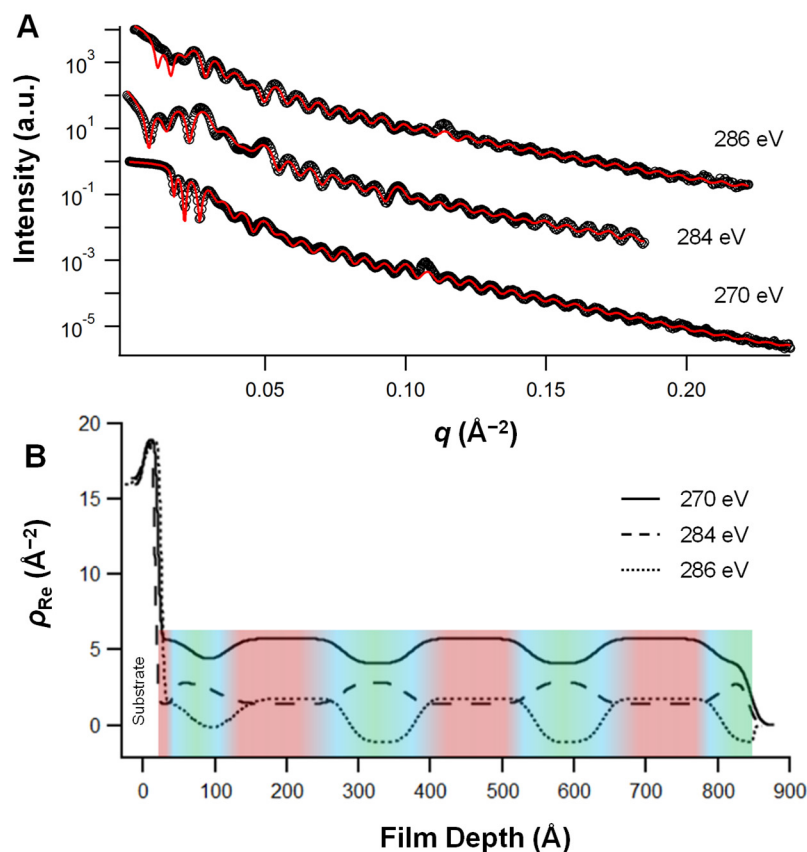


Figure 4.10: (A) Experimental (*black circles*) and simulated (*red lines*) reflectivity profiles determined for LSO-12 at three different energies: 286, 284, and 270 eV. (B) Composition profile for LSO-12 determined from reflectivity measurements. The red, green, and blue colors highlight the correspondence between each block and its SLD.

The real component of the SLD profile (ρ_R), determined from fits to the experimental data, is shown in Figure 4.10B for all three energies. Several models were tested while fitting the RSoXR data. First, an ABCBA-type model with a PEO layer isolated between PS layers was tested, representing the conventional LAM₃ morphology expected for triblock terpolymers. The LAM₃ model failed to fit the experimental data, eliminating the possibility that the material may organize differently in thin films compared to the bulk. Two other models, consistent with the LAMP morphology proposed in our previous work, were explored. The first model assumed an *explicit* PEO layer residing at the interface between the PS and PLA domains, while the second model incorporated an *implicit* PEO layer between the PS and PLA domains. The best fits for both models reduce to identical SLD

profiles where the PEO layer cannot be explicitly observed, indicating that a bilayer model accurately captures the measured SLD profile. The calculated profiles suggest that LSO-12 forms a lamellar morphology with a PS layer at the top surface followed by alternating domains of PS and PLA with PEO at the interfaces. Near the silicon substrate, the layers become less distinct and the interfaces become broader, potentially due to restricted motion at the surface.

In order to obtain greater insight into the results, SCFT calculations were employed to simulate $\rho_R(z)$. SCFT has been previously used to capture bottlebrush behavior by modifying the standard worm-like chain model to account for the strong steric interactions resulting from the highly grafted side chains.^{25,71-72} The composition profiles predicted by SCFT show excellent agreement with the experimental results (Figure 4.11).

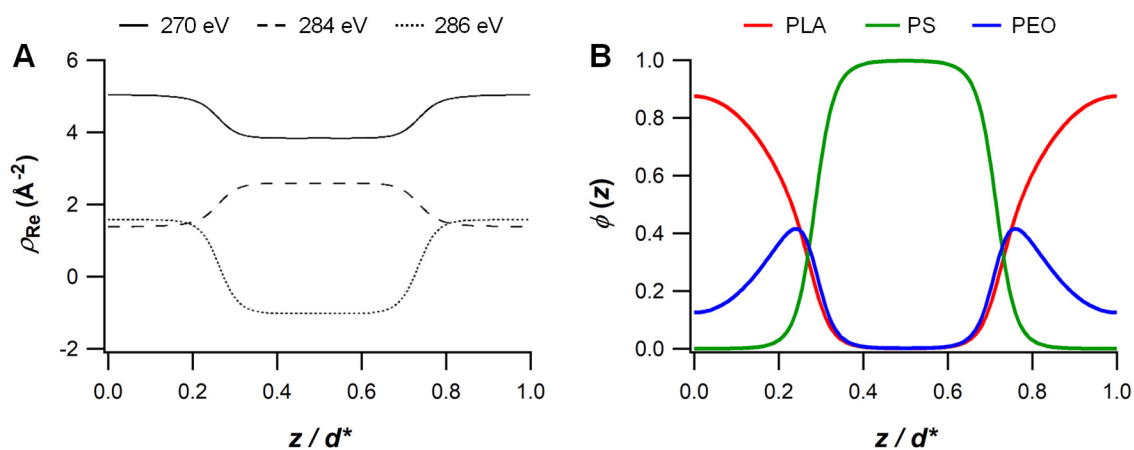


Figure 4.11: Composition profiles for LSO-12 determined by (A) fitting experimental reflectivity data or (B) SCFT. The relative segment concentrations of each component are provided over one normalized lamellar period (z/d^*). (A) Profiles were determined from RSoXR measurements at 270 eV (—), 284 eV (---), and 286 eV (.....); see Figure 4.10. (B) Profiles were calculated for PLA (red), PS (green), and PEO (blue). Comparison of reflectivity and SCFT profiles indicate close agreement between the measured and predicted results.

One surprising result that emerges from the reflectivity profiles is the presence of the PS block at the air interface. In order to evaluate the surface composition, NEXAFS measurements around the carbon edge were performed for LSO-12 and reference bottlebrush homopolymers (Figure 4.12). NEXAFS measurements were collected at the SXR beamline⁷³ of the Australian Synchrotron and corrected and normalized with QANT.⁷⁴ NEXAFS is an

analogous resonant soft X-ray spectroscopy that is highly sensitive to the chemical composition within the first 5 nanometers of a free surface. The LSO-12 NEXAFS spectra show a strong absorption peak at ≈ 285 eV, corresponding to the $1s \rightarrow \pi^*$ transition for the aromatic rings in polystyrene. A second distinct peak is observed at ≈ 288 eV, corresponding to the $1s \rightarrow \pi^*$ transition for the carbonyl bond in PLA. (A small peak is also present at 288 eV in the brush PS homopolymer reference sample, due to the bisimide linkages in the backbone of the brush and the methyl ester end group on the PS side chain.) Quantitative fitting of the LSO-12 spectrum suggests that there is ~ 80 % by volume of PS at the air interface, consistent with RSoXR analysis. Since NEXAFS is sensitive to several nanometers beneath the surface, some or all of the PLA and PEO in the signal likely originates beneath the PS layer. Because PS comprises the midblock of the brush LSO triblock, the backbones must be curved to allow PS to segregate to the surface. In other words, the ABC bottlebrush *must* form loops — analogous to flexible linear ABA' triblocks — despite the significant conformational and packing challenges looping imposes for the backbone and side chains. In fact, the composition of the surface layer and narrow thickness relative to a fully extended chain suggest that the surface layer is composed almost entirely of looped chains. The free energy penalty from these conformational effects is clearly outweighed by the enthalpic preference for mixing PLA and PEO chains ($\chi_{LO} \lesssim 0$).

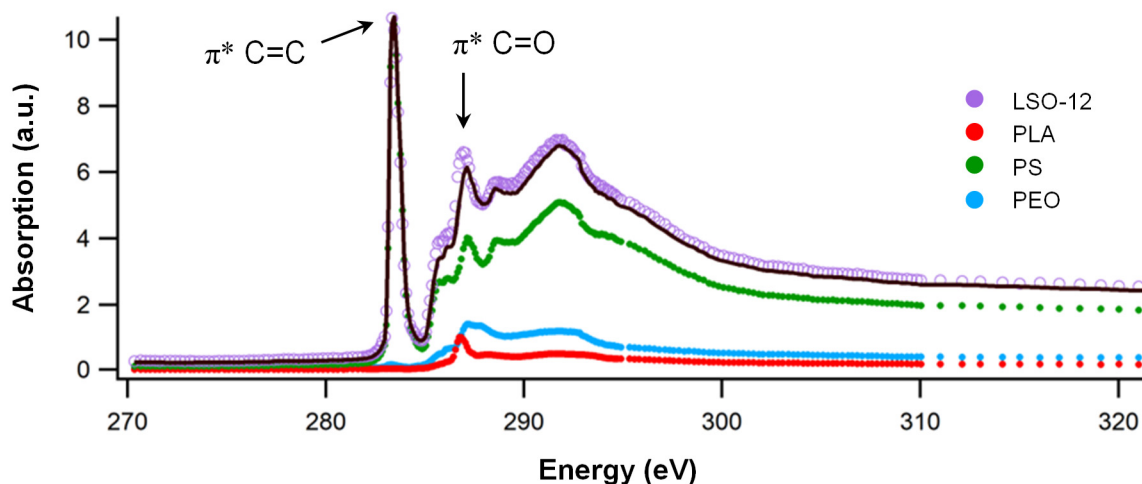


Figure 4.12: NEXAFS analysis of LSO-12 at the carbon edge. Arrows indicate transitions for PS ($C=C$ $1s \rightarrow \pi^*$ for the aromatic rings, $E = 284.5$ eV) and PLA ($C=O$ $1s \rightarrow \pi^*$ for the carbonyl, $E = 288$ eV).

Informed SCFT calculations provide further support for backbone curvature. Figure 4.13 shows the predicted distributions of PS and the polynorbornene backbone within one normalized period. The profiles indicate that the backbone concentration drops significantly in the center of the PS domain, then increases near the PS/PLA interface. This dip in the backbone concentration is consistent with a large fraction of the blocks forming loops. Reflectivity measurements at the nitrogen edge (407, 402, and 390 eV) were performed in attempts to experimentally determine the backbone distribution (that is, by tracking the bisimide functionality). However, the low nitrogen content (<1 wt%) and high absorptions coefficients did not allow resolution of the backbone concentration profile. Ongoing work aims to optimize the systems to enable determination of the backbone distribution, with the goal of additionally measuring the backbone *orientation*.

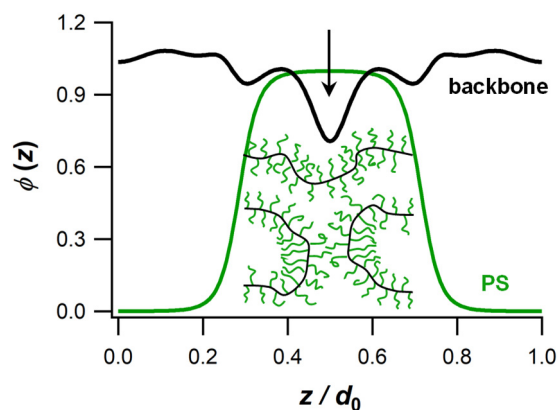


Figure 4.13: SCFT composition profile for LSO-12 within one normalized lamellar period (z / d^*), where $\phi(z)$ is the relative segment concentration. Calculated profiles for PS (*green*) and the backbone (*black*) are shown; PLA and PEO are not included. (See Figure 4.11B.) A schematic illustration of midblock configurations is provided. The arrow indicates a decrease in the backbone concentration at the center of the PS domain, suggesting a large fraction of looping midblocks.

Additional insight can be attained by examining trends in the lamellar periods and absolute domain thicknesses extracted from RSoXR measurements (Table 4.3). The overall changes in d^* with the backbone degree of polymerization of the PEO block closely agree with the d^* values determined from SAXS measurements of these materials in the bulk.⁷¹ The advantage of reflectivity is that the composition and thicknesses of individual layers can be directly interrogated. As N_C increases, the mixed PLA/PEO domain maintains a constant

thickness $d_{L+O} \approx 16.8$ nm, while the thickness of the PS domain decreases from 9.4 nm for LSO-8 to 6.5 nm for LSO-20. At the same time, the interfacial width increases from 3.8 nm to 7.5 nm. The data are compiled in Table 4.3, and a schematic illustration of chain configurations and relevant parameters is provided in Figure 4.14.

Table 4.3: Parameters resulting from the fits to the LSO reflectivity profiles. Uncertainties represent 95% confidence intervals determined by the directed evolution Monte Carlo Markov chain algorithm.⁷⁵

Sample	d^* (SAXS) (nm)	d^* (RSoXR) (nm)	d_S (nm)	d_{L+O} (nm)	Interfacial Width (nm)	PS Surface Thickness (nm)
LSO-8	26.8	26.1 ± 0.5	9.4 ± 0.3	16.7 ± 0.3	3.8 ± 0.5	4.6 ± 0.2
LSO-12	25.2	25.7 ± 0.6	8.8 ± 0.3	16.9 ± 0.3	4.5 ± 0.6	4.2 ± 0.3
LSO-16	24.6	25.2 ± 0.5	8.4 ± 0.3	16.8 ± 0.2	4.8 ± 0.8	3.8 ± 0.2
LSO-20	23.6	23.1 ± 0.5	6.5 ± 0.2	16.6 ± 0.3	7.5 ± 0.8	3.3 ± 0.2

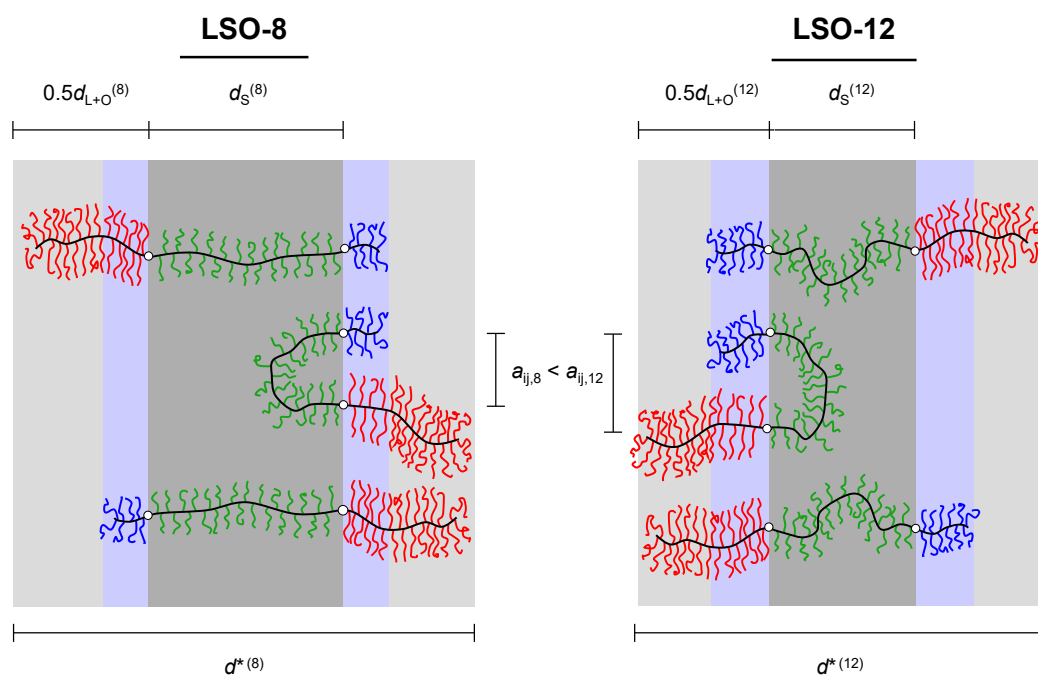


Figure 4.14: Schematic illustration of chain configurations over one lamellar period (d^*) for LSO-8 (left) and LSO-12 (right). Relevant length scales are indicated, including d^* , the thickness of the mixed PLA/PEO layers (d_{L+O}), the thickness of the PS layers (d_S), and the average distance between block junctions at the interface (a_{ij}).

The combination of these trends suggests that compatibilization at the interface is the primary factor motivating the unusual decrease in d^* with increasing total molecular weight. Blending PLA and PEO at the interface screens the unfavorable, high- χ interactions between PS and PLA. As increasingly longer PEO blocks are localized at the interface between domains, the average distance between block-block junctions (a_{ij}) increases. In order to maintain uniform melt density, d^* (the orthogonal length scale) must decrease.⁵⁵ This change in the cross-sectional area at the interface would typically reduce the thicknesses of both L/O and S domains, but it is offset here by the increasingly long PEO blocks anchored in the PLA-rich phases. Figure 4.15 highlights the relationship between d^* and a_{ij} .

Chain pullout has also been suggested as a reason for the period reduction in this system (Section 4-7): by analogy to linear ABA' triblock copolymers, when the end block lengths are sufficiently asymmetric, the shorter end blocks are expected to partially “pull out” into the B domains (Figure 4.7).^{51,53} While this mechanism may contribute in part to the d^* trend, it is inconsistent with the relative and absolute PLA and PS layer thicknesses determined by RSoXR. Furthermore, the SCFT calculations predict that the volume fraction of PEO at the center of the PS lamellae is only ~1% for LSO-8, reducing to nearly 0% in LSO-20. The small change in volume fraction is insufficient to effect the >10% change in d^* between LSO-8 and LSO-20. Finally, the relationship between the thickness of the PS surface layer and the interior PS layers suggest that there is a similarly large fraction of loops for those layers beneath the surface. For all samples, the thickness of the PS interior layers is slightly larger than twice the thickness of the surface layer. As the surface layer must be composed primarily of loops, this suggests a high fraction present in the interior layers as well. The correspondence between the thin film period determined by RSoXR and the bulk period from SAXS measurements indicate that this behavior is likely consistent across both thin films and bulk samples.

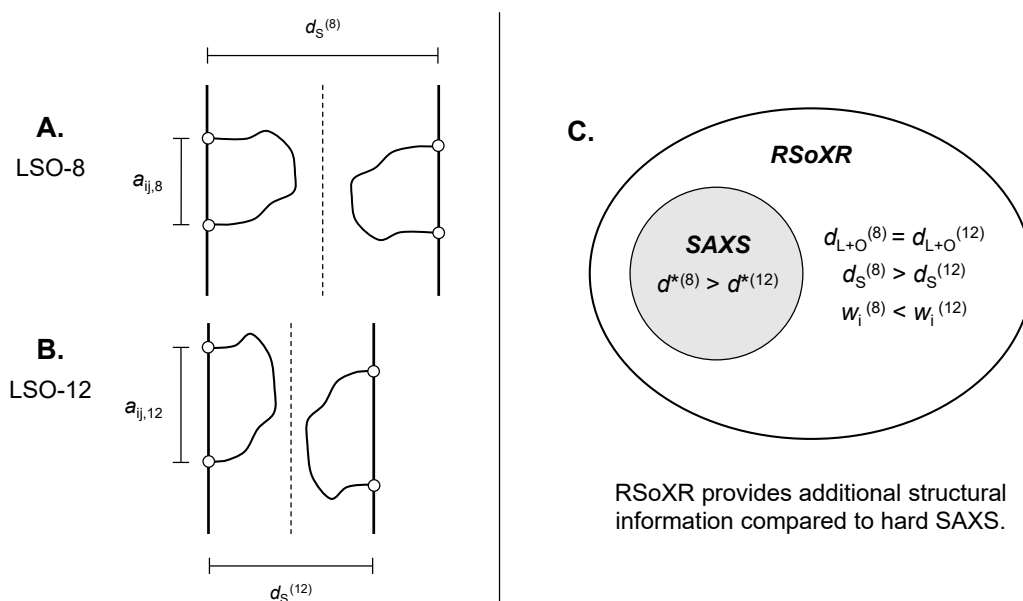


Figure 4.15: (A, B) Configurations of looping midblocks inferred from reflectivity measurements for (A) LSO-8 and (B) LSO-12; see also Figure 4.14. As N_C increases from 8 to 12, the thickness of the PS domain (d_s) decreases. A concomitant increase in the average distance between block junctions at the interface (a_{ij}) is expected. (C) Like SAXS, RSoXR enables determination of d^* . However, RSoXR provides additional information due to its sensitivity to chemical composition.

RSoXR and NEXAFS measurements demonstrate that bottlebrush block polymers can adopt a surprising degree of flexibility. The measurements demonstrate that, under certain conditions, the midblock in a bottlebrush triblock terpolymer is largely present at the air interface, providing evidence that the brush polymer forms loops despite the steric-induced stiffening of the backbone. The relationships between the thicknesses of this surface layer and the interior PS layers suggests that interior domains may also consist largely of looped configurations. This result raises interesting questions about *how* the side chains pack in looping midblocks and under what conditions curvature is allowed by the densely grafted polymer architecture. In linear block polymers, the ratio of looping and bridging blocks significantly impacts the mechanical performance and other physical properties. Further studies will explore how the midblock configuration influences the properties of bottlebrush block polymers. The unusual commensurability conditions (assembly at $3.25d^*$) will also be studied. Improving understanding of these phenomena will enable bottlebrush polymers to be better tailored for their many diverse potential applications.

4-11 Conclusions

The insights gained herein from both experiment and theory illustrate the profound influence low- χ interactions exert on self-assembly. Proper selection of χ_{ij} and f can generate unusual morphologies characterized by partial block mixing (LAMP), decouple molecular sequence from mesoscopic connectivity, and provide counterintuitive control over domain spacing. While high- χ block polymers have been the subject of widespread interest, low- χ systems remain relatively unexplored, yet the latter generate fascinating physics that are anticipated to gain importance as sequence complexity further evolves. Expanding the block polymer design toolkit to include low- χ interactions creates new opportunities to tailor mesoscale structure and should find utility in the future design of functional materials.

4-12 References

- (1) Thomas, E. L. *Science* **1999**, *286*, 1307.
- (2) Park, C.; Yoon, J.; Thomas, E. L. *Polymer* **2003**, *44*, 6725–6760.
- (3) Lutz, J.-F.; Ouchi, M.; Liu, D. R.; Sawamoto, M. *Science* **2013**, *341*, 628–637.
- (4) Bates, C. M.; Bates, F. S. *Macromolecules* **2016**, *50*, 3–22.
- (5) Leibler, L. *Macromolecules* **1980**, *13*, 1602–1617.
- (6) Bates, F. S.; Fredrickson, G. H. *Phys. Today* **1999**, *52*, 32–38.
- (7) Bates, F. S.; Hillmyer, M. A.; Lodge, T. P.; Bates, C. M.; Delaney, K. T.; Fredrickson, G. H. *Science* **2012**, *336*, 434–440.
- (8) Zheng, W.; Wang, Z.-G. *Macromolecules* **1995**, *28*, 7215–7223.
- (9) Bailey, T. S. Morphological behavior spanning the symmetric AB and ABC block copolymer states. University of Minnesota, 2001.
- (10) Xie, N.; Liu, M.; Deng, H.; Li, W.; Qiu, F.; Shi, A.-C. *J. Am. Chem. Soc.* **2014**, *136*, 2974–2977.
- (11) Gao, Y.; Deng, H.; Li, W.; Qiu, F.; Shi, A.-C. *Phys. Rev. Lett.* **2016**, *116*, 068304.
- (12) Legge, N. R. *Rubber Chem. Technol.* **1987**, *60*, 83–117.
- (13) Bluemle, M. J.; Zhang, J.; Lodge, T. P.; Bates, F. S. *Macromolecules* **2010**, *43*, 4449–4452.
- (14) Lee, S.; Bluemle, M. J.; Bates, F. S. *Science* **2010**, *330*, 349–353.
- (15) Lynd, N. A.; Oyerokun, F. T.; O’Donoghue, D. L.; Handlin, D. L.; Fredrickson, G. H. *Macromolecules* **2010**, *43*, 3479–3486.
- (16) Hashimoto, T.; Tanaka, H.; Hasegawa, H. *Macromolecules* **1990**, *23*, 4378–4386.
- (17) Matsen, M. W. *Macromolecules* **1995**, *28*, 5765–5773.
- (18) Kimishima, K.; Jinnai, H.; Hashimoto, T. *Macromolecules* **1999**, *32*, 2585–2596.
- (19) Tang, C.; Sivanandan, K.; Stahl, B. C.; Fredrickson, G. H.; Kramer, E. J.; Hawker, C. J. *ACS Nano* **2010**, *4*, 285–291.

- (20) Sveinbjörnsson, B. R.; Weitekamp, R. A.; Miyake, G. M.; Xia, Y.; Atwater, H. A.; Grubbs, R. H. *Proc. Natl. Acad. Sci. U.S.A.* **2012**, *109*, 14332–14336.
- (21) Bates, C. M.; Chang, A. B.; Momčilović, N.; Jones, S. C.; Grubbs, R. H. *Macromolecules* **2015**, *48*, 4967–4973.
- (22) Bates, C. M.; Chang, A. B.; Schulze, M. W.; Momčilović, N.; Jones, S. C.; Grubbs, R. H. *J. Polym. Sci., Part B: Polym. Phys.* **2016**, *54*, 292–300.
- (23) Radlauer, M. R.; Sinturel, C.; Asai, Y.; Arora, A.; Bates, F. S.; Dorfman, K. D.; Hillmyer, M. A. *Macromolecules* **2016**, *50*, 446–458.
- (24) Fredrickson, G. H. *The Equilibrium Theory of Inhomogeneous Polymers*; Oxford University Press: New York, 2006.
- (25) Dalsin, S. J.; Rions-Maehren, T. G.; Beam, M. D.; Bates, F. S.; Hillmyer, M. A.; Matsen, M. W. *ACS Nano* **2015**, *9*, 12233–12245.
- (26) Fetters, L. J.; Lohse, D. J.; Richter, D.; Witten, T. A.; Zirkel, A. *Macromolecules* **1994**, *27*, 4639–4647.
- (27) Dorgan, J. R.; Janzen, J.; Knauss, D. M.; Hait, S. B.; Limoges, B. R.; Hutchinson, M. H. *J. Polym. Sci., Part B: Polym. Phys.* **2005**, *43*, 3100–3111.
- (28) Olayo-Valles, R.; Lund, M. S.; Leighton, C.; Hillmyer, M. A. *J. Mater. Chem.* **2004**, *14*, 2729–2731.
- (29) Vayer, M.; Nguyen, T. H.; Sinturel, C. *Polymer* **2014**, *55*, 1048–1054.
- (30) Trent, J. S.; Scheinbeim, J. I.; Couchman, P. R. *Macromolecules* **1983**, *16*, 589–598.
- (31) Gai, Y.; Song, D.-P.; Yavitt, B. M.; Watkins, J. J. *Macromolecules* **2017**, *50*, 1503–1511.
- (32) Zalusky, A. S.; Olayo-Valles, R.; Wolf, J. H.; Hillmyer, M. A. *J. Am. Chem. Soc.* **2002**, *124*, 12761–12773.
- (33) Cochran, E. W.; Morse, D. C.; Bates, F. S. *Macromolecules* **2003**, *36*, 782–792.
- (34) Beardsley, T. M.; Matsen, M. W. *Phys. Rev. Lett.* **2016**, *117*, 217801.
- (35) Stadler, R.; Auschra, C.; Beckmann, J.; Krappe, U.; Voight-Martin, I.; Leibler, L. *Macromolecules* **1995**, *28*, 3080–3097.
- (36) Balsamo, V.; Gil, G.; Urbina de Navarro, C.; Hamley, I. W.; von Gyldenfeldt, F.; Abetz, V.; Cañizales, E. *Macromolecules* **2003**, *36*, 4515–4525.
- (37) Liu, M.; Li, W.; Qiu, F.; Shi, A.-C. *Macromolecules* **2012**, *45*, 9522–9530.
- (38) Bailey, T. S.; Hardy, C. M.; Epps, T. H.; Bates, F. S. *Macromolecules* **2002**, *35*, 7007–7017.
- (39) Meuler, A. J.; Ellison, C. J.; Qin, J.; Evans, C. M.; Hillmyer, M. A.; Bates, F. S. *J. Chem. Phys.* **2009**, *130*, 234903.
- (40) Bailey, T. S.; Pham, H. D.; Bates, F. S. *Macromolecules* **2001**, *34*, 6994–7008.
- (41) Couchman, P. R. *Macromolecules* **1978**, *11*, 1156–1161.
- (42) Gaikwad, A. N.; Wood, E. R.; Ngai, T.; Lodge, T. P. *Macromolecules* **2008**, *41*, 2502–2508.
- (43) Younes, H.; Cohn, D. *Eur. Polym. J.* **1988**, *24*, 765–773.
- (44) Sheth, M.; Kumar, R. A.; Davé, V.; Gross, R. A.; McCarthy, S. P. *J. Appl. Polym. Sci.* **1997**, *66*, 1495–1505.
- (45) Sioula, S.; Hadjichristidis, N.; Thomas, E. L. *Macromolecules* **1998**, *31*, 5272–5277.
- (46) Tang, P.; Qiu, F.; Zhang, H.; Yang, Y. *J. Phys. Chem. B* **2004**, *108*, 8434–8438.

- (47) Frielinghaus, H.; Hermsdorf, N.; Almdal, K.; Mortensen, K.; Messé, L.; Corvazier, L.; Fairclough, J. P. A.; Ryan, A. J.; Olmsted, P. D.; Hamley, I. W. *Europhys. Lett.* **2001**, *53*, 680–686.
- (48) Chatterjee, J.; Jain, S.; Bates, F. S. *Macromolecules* **2007**, *40*, 2882–2896.
- (49) Mao, H.; Hillmyer, M. A. *Macromol. Chem. Phys.* **2008**, *209*, 1647–1656.
- (50) Lai, W.-C.; Liao, W.-B.; Lin, T.-T. *Polymer* **2004**, *45*, 3073–3080.
- (51) Matsen, M. W. *J. Chem. Phys.* **2000**, *113*, 5539–5544.
- (52) Milner, S. T.; Witten, T. A. *J. Phys. France* **1988**, *49*, 1951–1962.
- (53) Hamersky, M. W.; Smith, S. D.; Gozen, A. O.; Spontak, R. J. *Phys. Rev. Lett.* **2005**, *95*, 168306.
- (54) Smith, S. D.; Hamersky, M. W.; Bowman, M. K.; Rasmussen, K. Ø.; Spontak, R. J. *Langmuir* **2006**, *22*, 6465–6468.
- (55) Winey, K. I.; Thomas, E. L.; Fetters, L. J. *Macromolecules* **1991**, *24*, 6182–6188.
- (56) Koizumi, S.; Hasegawa, H.; Hashimoto, T. *Macromolecules* **1994**, *27*, 7893–7906.
- (57) Chen, S.-C.; Kuo, S.-W.; Jeng, U. S.; Su, C.-J.; Chang, F.-C. *Macromolecules* **2010**, *43*, 1083–1092.
- (58) Fredrickson, G. H. *Macromolecules* **1993**, *26*, 2825–2831.
- (59) Mikhaylov, I. V.; Darinskii, A. A. *Polym. Sci. Ser. A* **2015**, *57*, 239–250.
- (60) Zhulina, E. B.; Halperin, A. *Macromolecules* **1992**, *25*, 5730–5741.
- (61) Kane, L.; Spontak, R. J. *Macromolecules* **1994**, *27*, 1267–1273.
- (62) Matsen, M. W.; Thompson, R. B. *J. Chem. Phys.* **1999**, *111*, 7139–7146.
- (63) Lin, T.-P.; Chang, A. B.; Luo, S.-X.; Chen, H.-Y.; Lee, B.; Grubbs, R. H. *ACS Nano* **2017**, *11*, 11632–11641.
- (64) Wang, C.; Araki, T.; Ade, H. *Appl. Phys. Lett.* **2005**, *87*, 214109.
- (65) Sunday, D. F.; Kline, R. J. *Macromolecules* **2015**, *48*, 679–686.
- (66) Rosenberg, R. A.; Love, P. J.; Rehn, V. *Phys. Rev. B* **1986**, *33*, 4034–4037.
- (67) Patel, S. N.; Su, G. M.; Luo, C.; Wang, M.; Perez, L. A.; Fischer, D. A.; Prendergast, D.; Bazan, G. C.; Heeger, A. J.; Chabinyc, M. L.; Kramer, E. J. *Macromolecules* **2015**, *48*, 6606–6616.
- (68) Virgili, J. M.; Tao, Y.; Kortright, J. B.; Balsara, N. P.; Segalman, R. A. *Macromolecules* **2007**, *40*, 2092–2099.
- (69) Sunday, D. F.; Hammond, M. R.; Wang, C.; Wu, W.-l.; DeLongchamp, D. M.; Tjio, M.; Cheng, J. Y.; Pitera, J. W.; Kline, R. J. *ACS Nano* **2014**, *8*, 8426–8437.
- (70) Ferron, T.; Pope, M.; Collins, B. A. *Phys. Rev. Lett.* **2017**, *119*, 167801.
- (71) Chang, A. B.; Bates, C. M.; Lee, B.; Garland, C. M.; Jones, S. C.; Spencer, R. K. W.; Matsen, M. W.; Grubbs, R. H. *Proc. Natl. Acad. Sci. U.S.A.* **2017**, *114*, 6462–6467.
- (72) Kawamoto, K.; Zhong, M.; Gadelrab, K. R.; Cheng, L.-C.; Ross, C. A.; Alexander-Katz, A.; Johnson, J. A. *J. Am. Chem. Soc.* **2016**, *138*, 11501–11504.
- (73) Cowie, B. C. C.; Tadich, A.; Thomsen, L. *AIP Conf. Proc.* **2010**, *1234*, 307–310.
- (74) Gann, E.; McNeill, C. R.; Tadich, A.; Cowie, B. C. C.; Thomsen, L. *J. Synchrotron Radiat.* **2016**, *23*, 374–380.
- (75) Dura, J. A.; Richter, C. A.; Majkrzak, C. F.; Nguyen, N. V. *Appl. Phys. Lett.* **1998**, *73*, 2131–2133.